Journal of Engineering Mechanics and Machinery (2026)
Clausius Scientific Press, Canada

DOI: 10.23977/jemm.2026.110209
ISSN 2371-9133 Vol. 11 Num. 2

Mechanical Property Analysis of Periodic Hierarchical Porous Composite Structures

Changxin Lin*

School of Mechanical Engineering, University of Shanghai for Science and Technology, Shanghai, 200093, China
2606041125@qq.com
**Corresponding author*

Keywords: Periodic hierarchical porous structure; In-plane compression; Out-of-plane compression; Energy absorption performance

Abstract: Periodic hierarchical porous structures possess advantages such as lightweight, high load-bearing capacity, and good energy absorption, making them promising for applications in buffer protection and lightweight load-bearing applications. This paper selects four structures, establishes in-plane and out-of-plane compression models, and conducts comparative analysis under unified conditions. The mechanical properties are evaluated through force-displacement curves, considering peak force, average compressive force, total energy absorption, and load efficiency. The results show that the structural configuration and loading direction significantly affect the deformation mode and mechanical response. Different structures exhibit differences in load-bearing capacity and energy absorption: some structures have high multi-directional load-bearing capacity, some show significant load-bearing enhancement during the compaction stage, some have relatively balanced responses, while a few structures have lower load-bearing capacity and require further optimization. The research results can provide a reference for the design of related structures.

1. Introduction

With the increasing demands for lightweight and safety performance in fields such as aerospace, vehicle engineering, rail transportation, and protective equipment, traditional solid structures struggle to simultaneously achieve low mass, high load-bearing capacity, and efficient energy absorption [1]. Porous structures, with their lower overall density and controllable pore morphology, unit arrangement, and connection methods, can improve load-bearing and buffering energy absorption performance while reducing structural mass. Inspired by natural porous tissues such as wood, honeycomb, skeleton, and plant stems, regularized, periodic, and hierarchical designs have gradually been introduced into engineering structures, forming honeycomb, lattice, and periodic hierarchical porous structures, providing new ideas for the design of lightweight load-bearing and safety protection structures [2].

Periodic structures, as typical porous metamaterials, have attracted widespread attention in the field of collision protection due to their unique geometric properties. Recent studies have highlighted their enormous potential in crashworthiness applications. Li et al. [3] investigated the static compression and dynamic impact performance of PRST and IRST AlSi10Mg metamaterials, demonstrating that coordinated tuning of topology and dual-strut diameters enables adjustable stiffness and enhanced load-bearing and energy absorption at low volume fractions. Tao et al. [4] developed a 4D-printed multistable mechanical metamaterial with reconfigurable geometry, deployable functionality, and tunable mechanical properties, demonstrating its programmable deformation, shape recovery, and adaptability through microstructural gradients and composite design. Chen et al. [5] studied reversible negative-stiffness mechanical metamaterials for high energy dissipation and low-frequency vibration suppression, revealing that their hysteretic phase-transition behavior enables stable energy dissipation and effective vibration mitigation. Li et al. [6] examined an origami-inspired mechanical metamaterial with programmable anisotropic compression behavior, demonstrating distinct folding, buckling, and graded deformation modes that enable direction-dependent stiffness and energy absorption. Akamatsu et al. [7] evaluated a topology-optimized two-dimensional cavity-free mechanical metamaterial with a negative coefficient of thermal expansion, demonstrating through homogenization and numerical analysis that negative thermal expansion can be achieved without internal cavities. Mizzi et al. [8] investigated additively manufactured chiral honeycombs derived from Euclidean multi-polygonal tessellations, revealing tunable Poisson's ratios and stiffnesses together with distinctive sequential layer-by-layer collapse modes under compression. Lyu et al. [9] assessed a mechanical metamaterial with a sign-switchable Poisson's ratio and tunable stiffness, demonstrating negative Poisson's ratio in tension, positive Poisson's ratio in compression, and pronounced tension–compression stiffness asymmetry induced by self-contact. Luo et al. [10] developed a TPMS-based strut–shell interpenetrating lattice metamaterial with widely tunable mechanical properties and controllable anisotropy, demonstrating that mutual support between the interpenetrating lattices stabilizes post-failure deformation and enhances energy absorption by up to 74%. Wang et al. [11] analyzed flexible mechanical metamaterials with tunable elastic properties, demonstrating broad adjustability in stiffness and Poisson's ratio together with enhanced deformability, sensitivity, and auxeticity compared with conventional star-shaped cellular structures.

This paper takes periodic hierarchical porous structures as the research object, establishes in-plane and out-of-plane compression finite element models, and focuses on analyzing the influence of structural configuration and loading direction on load-bearing capacity, energy absorption performance, and deformation stability. By comparing the force-displacement response and energy absorption characteristics of different structures during local bending, member buckling, element collapse, and progressive compaction processes, the differences in their compressive mechanical properties are revealed.

2. Mechanical response characteristics

The impact resistance of porous structures primarily reflects their energy absorption and load transfer characteristics under impact loads. During a collision, the structure dissipates external energy through plastic deformation, local buckling, and element collapse. An ideal energy-absorbing structure should not only possess high energy absorption capacity but also effectively suppress the initial peak load, reducing the impact force and deceleration transmitted to occupants or protected components. To comprehensively characterize the impact resistance of a structure, a series of mechanical indicators are typically used to quantitatively evaluate its load-bearing capacity, energy absorption efficiency, and load stability, as shown in Figure 1, mainly including:

Peak Crushing Force (PCF) represents the maximum load a structure can withstand during a collision or compression. An excessively high PCF can subject occupants to significant impact forces and deceleration in a short period, increasing the risk of injury. Therefore, in the design of energy-absorbing structures, this indicator is typically kept within a safe threshold.

Mean Crushing Force (MCF) represents the average load a structure experiences throughout the compression process and can be used to measure its sustained load-bearing capacity. Its mathematical expression is:

$$MCF = \frac{\int_0^d F(x)dx}{d} \quad (1)$$

Where d is the crushing displacement and $F(x)$ is the instantaneous impact force.

Crushing Force Efficiency (CFE) characterizes the degree of matching between the average load-bearing capacity and the peak load of a structure, and its value is typically between 0 and 1. A higher CFE indicates that the structure can maintain a higher and more stable load-bearing capacity under lower peak loads. Its expression is:

$$CFE = \frac{MCF}{PCF} \quad (2)$$

Total energy absorption (EA) represents the total energy dissipated by a structure during the entire compression or collision process through irreversible behaviors such as plastic deformation, buckling, and collapse. Its expression is:

$$EA = \int_0^d F(x)dx \quad (3)$$

Specific Energy Absorption (SEA) represents the energy absorbed per unit mass of a structure, used to measure the balance between its energy absorption capacity and its lightweight level. A higher SEA indicates that the structure can dissipate more energy with a lower mass, and the material utilization efficiency is also higher. Its mathematical expression is:

$$SEA = \frac{EA}{m} \quad (4)$$

Where m is the total mass of the structure.

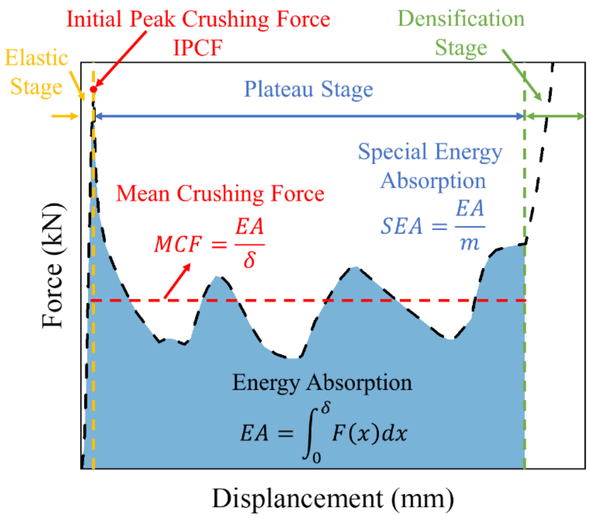

Figure 1: Schematic diagram of the impact force response of porous materials under load

3. Finite element simulation results and analysis

3.1. Finite element model

This paper establishes a periodic hierarchical porous structure and creates in-plane and out-of-plane compression finite element models in simulation software, as shown in Figure 2. Each model consists of an upper pressure plate, a lower pressure plate, and a middle porous structure, where the porous structure is the main load-bearing and energy-absorbing region, and the upper and lower pressure plates are used to apply loads and provide constraints. The porous material is made of 316L stainless steel, and the material parameters are shown in Table 1.

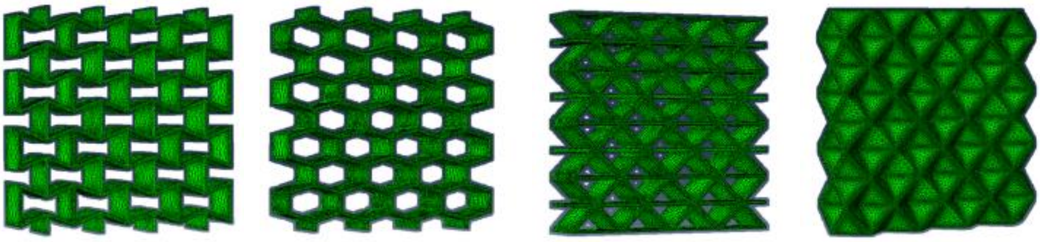

Figure 2: Finite element model of porous materials

The pressure plate and the porous structure are in surface-to-surface contact. The normal direction is set to prevent mutual penetration, and the tangential direction is set to describe the interfacial friction. The model uses the same contact parameters to ensure the comparability of the results. Considering that the rod and the hole wall may come into contact, be squeezed, and close the pores during large deformation, the model also considers the contact behavior inside the porous structure to avoid local penetration and reasonably reflect the load increase during the compaction stage.

Table 1: The chemical compositions of 316L stainless steel.

Element	Ni	Cr	Mo	C	Mn	Fe
Wt.%	10-14	16-18	2-3	≤0.03	≤2.0	Balance

The upper and lower pressure plates are controlled by reference points RP-1 and RP-2, respectively. To clearly illustrate the loading and constraint methods, Figure 3 omits non-essential information such as the pressure plate mesh and local coordinates from the actual model, retaining only the pressure plates, the specimen, the reference points, and the loading direction. The lower pressure plate reference point RP-2 constrains all translational and rotational degrees of freedom, while the upper pressure plate reference point RP-1 applies displacement along the compression direction and restricts translational and rotational movements in other non-loading directions to prevent offset during loading, as shown in Figure 3.

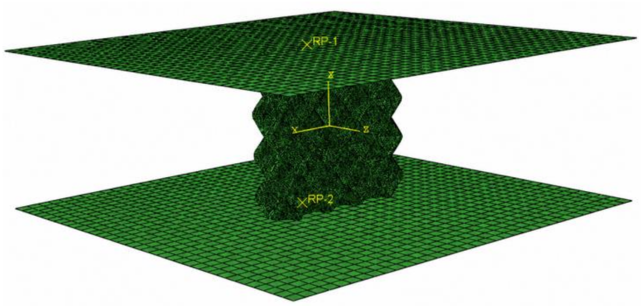

Figure 3: Assembly drawing of pressure plate and porous material in finite element model

Both in-plane and out-of-plane compression employ a method of fixing the lower pressure plate and applying displacement with the upper pressure plate. The in-plane compression direction corresponds to approximately 5 mm of structural height, with a compression displacement of 3.5 mm; the out-of-plane compression direction corresponds to approximately 20 mm of structural height, with a compression displacement of 14 mm. Both conditions achieve approximately 70% compression. For the same model number, the central porous structure remains unchanged; only the position and direction of the pressure plates are adjusted.

3.2. Results analysis

To further observe the local stress changes of different in-plane models during compression, this section selects the Von Mises equivalent stress distribution results of four groups of in-plane models at typical moments for comparative analysis. Stress cloud maps were extracted for each model at the initial state, mid-compression, and near the end of compression to reflect the stress concentration locations and overall deformation trends of the structure from the start of contact, gradual deformation to the end of compression, as shown in Figure 4.

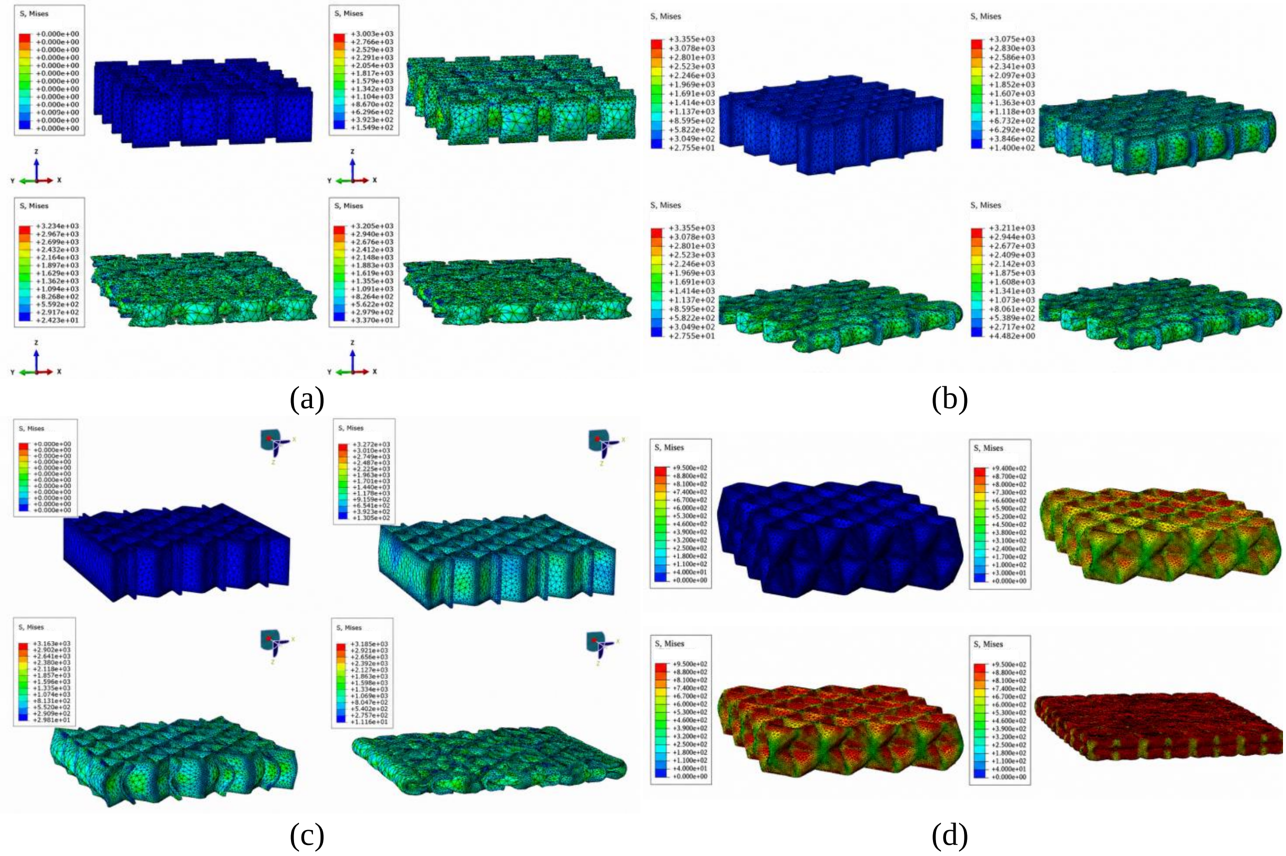

Figure 4: In-plane compression stress contour plot: (a) Model 1, (b) Model 2, (c) Model 3, (d) Model 4

In-plane model 1 exhibits low initial stress, which concentrates on the upper surface and connections during compression and then expands outwards. At termination, the stress is distributed across the contact surface, edges, and collapse area, without forming a single instability point, demonstrating a gradual expansion characteristic. In-plane model 2 also exhibits low initial stress. Subsequently, lateral and internal elements participate in load bearing, forming continuous stress bands that gradually expand in the middle and later stages. At termination, the stress still maintains a large distribution area, reflecting multi-element collaborative load bearing. In-plane model 3 shows stress expanding from the contact area towards the surface, edges, and interior. In the middle and later stages, the stress is dispersed across multiple elements, concentrating at the connection and contact areas at termination, without significant single-point concentration, indicating relatively uniform load transfer. In-plane model 4 initially concentrates stress at corrugated protrusions and transitions, then expands to the surface and lateral areas. At termination, the stress is mainly distributed on the upper contact surface and support area, exhibiting obvious compaction characteristics. The stress scales differ, requiring a comprehensive assessment combining numerical values and curves.

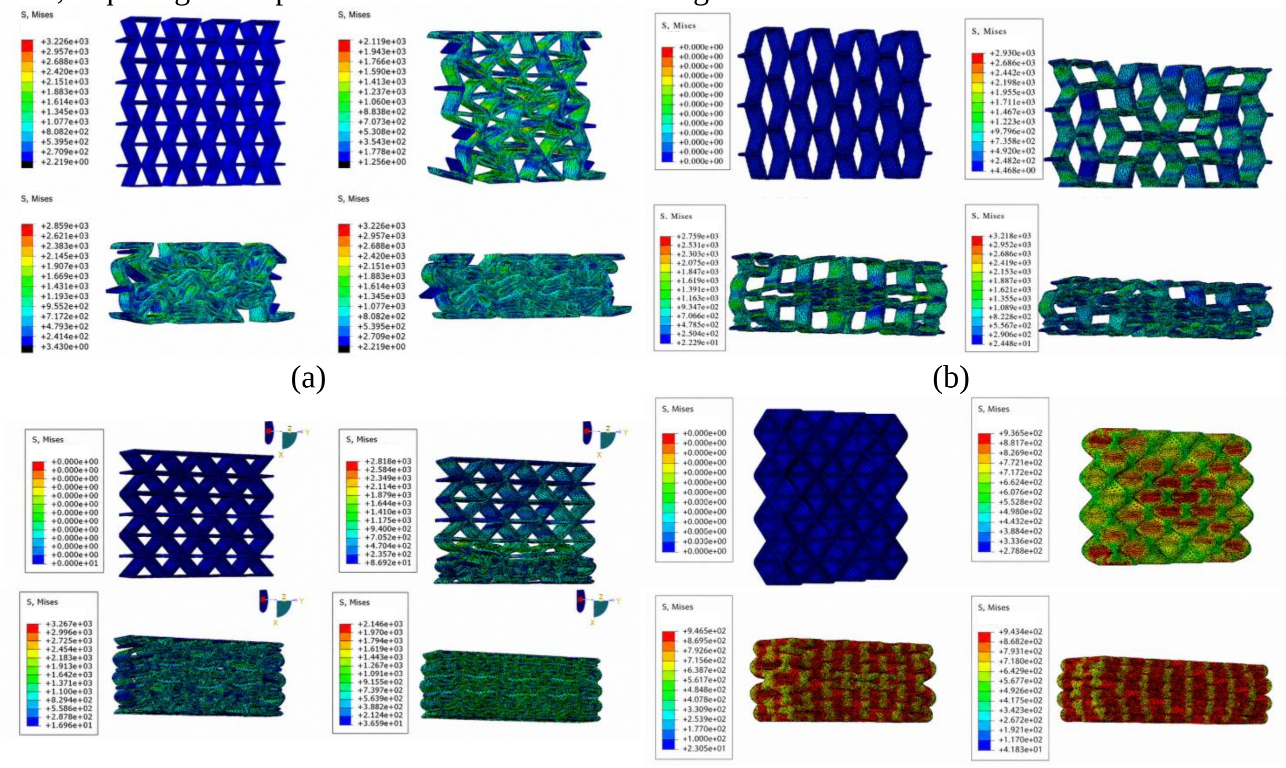

(a) (b) (c) (d)

Figure 5: Out-plane compression stress contour plot: (a) Model 1, (b) Model 2, (c) Model 3, (d) Model 4

The out-plane model 1 initially experienced low stress, followed by local buckling and bending in the lower elements, with deformation gradually expanding to the entire structure. In the mid-to-late stages, the structure exhibited extensive folding, contact, and compression, with stress concentrated mainly at folding corners and member contact areas. Upon termination, it entered a distinct densification stage, displaying clear layered collapse characteristics. The out-plane model 2 maintained a relatively intact skeleton shape in the early stages of compression, primarily through member bending and local rotation to coordinate deformation. As loading progressed, some cells gradually flattened and came into contact, but the original configuration remained partially identifiable. Its collapse process was relatively smooth, exhibiting progressive crushing characteristics, which helped maintain a relatively stable load-bearing response. The out-plane model 3 exhibited a more pronounced staged collapse. In the early stages of compression, the lower region unstable first, while the upper part retained some integrity. Subsequently, a large number of elements stacked and compressed, and the structure quickly transitioned to densification. Compared to out-of-plane model 1, its collapse progressed faster and it was more sensitive to local instability. The high-stress areas in the out-plane 4 model are relatively dispersed, mainly located in the contact and transition regions of repeating elements, without forming obvious single-point concentrations. As compression progresses, the structure gradually flattens, internal contact strengthens, and the stress distribution tends to be continuous, indicating that load transfer is mainly achieved through the coordinated deformation of a large range of elements. However, the actual load-bearing capacity still needs to be comprehensively judged in conjunction with the force-displacement curve, as shown in Figure 5.

The four curves in Figure 6 all exhibit significant nonlinearity, indicating that in-plane compression is accompanied by deformations such as local bending, buckling, contact compression, and pore compaction. In the initial loading stage, the reaction force gradually increases with the contact of the pressure plates, mainly corresponding to the initial load-bearing capacity and local elastic deformation of the structure. Subsequently, buckling and compression occur sequentially in the internal members, pore walls, and connecting areas, and the curves enter a fluctuating stage, reflecting the gradual collapse and continuous energy absorption process of the porous structure.

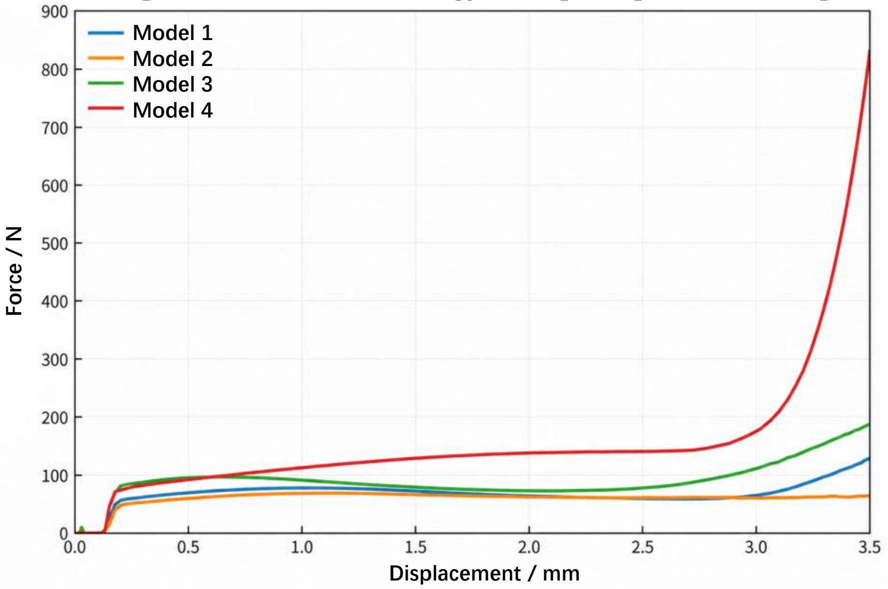

Figure 6: Force-displacement curves of in-plane model

The reaction force of model 1 in-plane gradually increases with displacement and fluctuates to a certain extent, indicating that the internal elements participate in the load-bearing capacity sequentially. Its curve characteristics are consistent with the gradual deformation process of stress spreading from local areas to the surrounding areas. Model 2 in-plane shows relatively stable overall changes and small fluctuation amplitudes, indicating good continuity in its compression process without significant sudden increases or decreases, and exhibiting a relatively stable load response. Model 3 in-plane shows a continuous increase in load-bearing capacity in the middle and later stages, indicating that multiple support elements participate in load transfer together, and the internal load-bearing path continuously plays a role in the compression process. Model 4 in-plane shows significantly higher reaction force levels and peak values, mainly related to its strong structural continuity, larger effective load-bearing area, and earlier compaction effect. Based on the stress cloud diagram, it can be seen that the high stress area is widely distributed. Therefore, the higher peak force mainly comes from the expansion of the overall bearing range, rather than a single local stress concentration.

As shown in Figure 7, all four models exhibit significant nonlinear responses during out-of-plane compression, but their load-bearing capacities differ considerably. Out-of-plane model 1 shows a low initial reaction force, gradually increasing after approximately 10 mm of displacement, and then entering a compaction strengthening stage, with a peak value of approximately 21.60 kN. This indicates that its initial deformation is mainly dominated by progressive deformation and local buckling of structural elements. Out-of-plane model 2 has the lowest overall load-bearing capacity, with a peak value of only approximately 5.90 kN. Its curve is relatively flat for most of the compression stage, indicating weak out-of-plane support and limited compaction strengthening effect. Out-of-plane model 3 has a peak value of approximately 39.05 kN. The early curve shows some fluctuations, reflecting the successive instability and contact reorganization of local elements. After the displacement exceeds approximately 11 mm, the reaction force increases rapidly, demonstrating strong late-stage compaction bearing capacity. In comparison, the out-of-plane model 4 exhibits the best overall load-bearing performance, with a peak load of 88.38 kN. It can generate a high reaction force in the early stage of compression and shows significant compaction strengthening characteristics after about 12 mm, indicating that the structure can establish an effective load-bearing path earlier and has the strongest out-of-plane compressive strength.

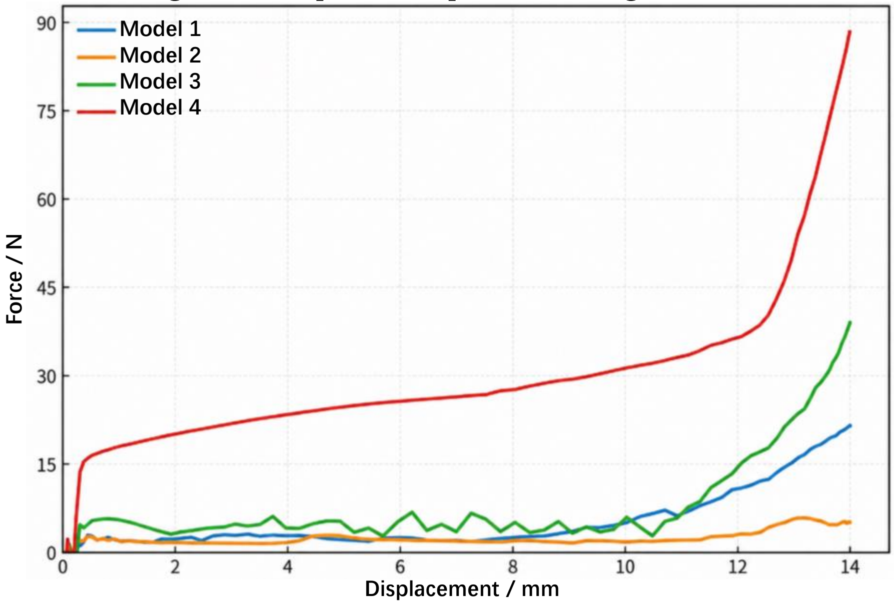

Figure 7: Force-displacement curves of out-plane model

4. Conclusion

This paper establishes four sets of in-plane and out-of-plane compression finite element models of periodic hierarchical porous structures, and analyzes their deformation behavior, force-displacement response, and energy absorption performance under unified material parameters, contact conditions, and compression ratios. The results show that all four models exhibit significant nonlinear characteristics during compression, sequentially undergoing stages of local buckling, element folding, pore closure, and compaction. Different configurations show significant differences in stress concentration locations, collapse propagation paths, and final compaction morphology, indicating that the compressive performance of the structure is closely related to the internal pore arrangement and element connection method.

Under in-plane compression conditions, the peak forces of each model are 128.98, 68.68, 187.71, and 831.26 kN, respectively. Model 4 has the strongest load-bearing capacity, followed by Model 3, and Model 2 has the lowest. Under out-of-plane compression, the peak forces of each model were 21.60, 5.90, 39.05, and 88.38 kN, respectively. Model 4 also exhibited the strongest thickness-direction support and compaction strengthening capacity, Model 3 showed good potential for later-stage load bearing, while Model 2 had relatively weak overall support. Overall, the load bearing capacity of the four models under both in-plane and out-of-plane compression was ranked as follows: Model 4, Model 3, Model 1, and Model 2, indicating that the structural configuration has a significant impact on the compressive load bearing performance of periodic hierarchical porous structures.

References

[1] Khalid M Y, Arif Z U, Tariq A, et al. 3D printing of active mechanical metamaterials: A critical review[J]. Materials

& Design, 2024, 246: 113305.
[2] Liu K, Han L, Hu W, et al. 4D printed zero Poisson's ratio metamaterial with switching function of mechanical and vibration isolation performance[J]. Materials & Design, 2020, 196: 109153.
[3] Li Z, Chen Z, Dou Z, et al. Design and evaluation of TPMS-inspired lightweight metamaterials with tunable quasi-static and dynamic mechanical performance[J]. Thin-Walled Structures, 2026: 114609.
[4] Tao R, Xi L, Wu W, et al. 4D printed multi-stable metamaterials with mechanically tunable performance[J]. Composite Structures, 2020, 252: 112663.
[5] Chen S, Liu X, Hu J, et al. Elastic architected mechanical metamaterials with negative stiffness effect for high energy dissipation and low frequency vibration suppression[J]. Composites Part B: Engineering, 2023, 267: 111053.
[6] Li M, Chen H, Ma J, et al. An origami metamaterial with distinct mechanical properties in three orthotropic directions[J]. International Journal of Mechanical Sciences, 2024, 283: 109713.
[7] Akamatsu D, Matsushima K, Yamada T. Optimal design of cavity-free mechanical metamaterials exhibiting negative thermal expansion[J]. International Journal of Mechanical Sciences, 2024, 283: 109693.
[8] Mizzi L, Simonetti A, Spaggiari A. Mechanical properties and failure modes of additively-manufactured chiral metamaterials based on Euclidean tessellations: an experimental and finite element study[J]. Rapid Prototyping Journal, 2024, 30(11): 59-71.
[9] Lyu Y, Song X, Wang H, et al. A novel mechanical metamaterial with tunable stiffness and individually adjustable poisson's ratio[J]. Materials Today Communications, 2024, 40: 110135.
[10] Luo Z, Tang Q, Song J, et al. TPMS-based strut-shell interpenetrating lattice metamaterial with wide-range customizable mechanical properties and superior energy absorption[J]. Composite Structures, 2024, 349: 118555.
[11] Wang S, Guo J, Biczo A, et al. Design and macroscopic mechanical responses of auxetic metamaterials with tunable stiffness[J]. Materials & Design, 2024, 241: 112913.